STIFFNESS METAMODELLING OF 2D BOLTED EXTENDED END-PLATE STEEL CONNECTIONS USING MODAL DECOMPOSITION

Javier Gracia
University of Oviedo. Spain.
Rufino Goñi,
University of Navarra. Spain
Eduardo Bayo,
University of Navarra. Spain

ABSTRACT

The accurate simulation of steel structures requires a precise model of the joint behaviour. The methods proposed by the steel codes are based on either rotating springs or involved models of springs and rigid bars. In this article, a precise method to model the stiffness of 2D bolted steel connections is presented. First, the joint is accurately modelled using finite elements (FE). Then, the FE model is condensed to a cruciform element of 4 nodes (12 degrees of freedom) by constraining each side cross-section to a node located at its centre of gravity. Subsequently, forces are applied to each node to compute the flexibility matrix, which is then used to construct the stiffness matrix that is finally decomposed through singular value factorization. Following this procedure, a parametric study is conducted to build the training and validation sets of the metamodel. Kriging and Radial Basis Functions are chosen to metamodel and predict the stiffness matrices of the cases not included in the parametric study. Finally, steel structures are analysed with both complete finite elements and surrogate models, and the results are used to confirm the accuracy of the proposed method.

Keywords: Steel connections; structural analysis; cruciform finite elements; modal analysis; metamodel; Kriging and Radial Basis Functions

1 INTRODUCTION

Modern analysis procedures, introduced in current structural codes [1–3], are used to model the complex behaviour of steel joints and frames. The common assumption of considering the joints as pinned (zero stiffness) or fully rigid (infinite stiffness) is receding due to the need of considering the real stiffness of the joints when performing frame analyses. In addition, the characterization of the joint stiffness is essential to classify them as pinned, rigid or semi-rigid.

The standard approach to model steel joints is by means of rotational springs of zero-length attached at the intersection of the beam and column. Different formulations have been proposed for these springs: the power model [4], the Frye-Morris polynomial [5] and the Eurocode 3 (EC3) [2] approach, among others. The EC3 method provides rules and formulae to transform each part of the joint into a translational spring (component). Then, these components are assembled into a mechanical model to represent the full joint. Finally, the model is condensed and transformed into two rotational springs of zero-length attached at each side of the joint.

Although all these formulations provide reasonable approximations, they do not take into account the whole and complex behaviour that occurs at the joint. The column panel deformation, due to bending moments and shear forces, is not directly considered. The column panel has been extensively studied [6–11], and all research has reached similar conclusions: the behaviour of the web panel is critical for all the limiting states of frame analyses. In this regard, the zero-length rotational spring model does not account for the real dimensions of the joint, which affect the magnitude of the forces acting at the joint. Moreover, this model is not capable of considering the interaction of bending moments and shear forces in the panel zone. In order to circumvent this problem EC3 proposes the transformation parameter β whose value is calculated from the forces acting at the joint. A drawback of this procedure is that those forces are not known until the frame analysis is performed, and consequently an iterative procedure is necessary to converge to the correct values [12].

One way to avoid the transformation parameter is by considering the full mechanical model (composed of rigid bars and springs) of each joint within the frame analysis as proposed in [13]. In this way, the real dimensions of the joint are considered, but other drawbacks arise. As the links are rigid, bending and axial deformations of the column are constrained, and in addition the rigid links may lead to ill conditioning of the frame stiffness matrix. Furthermore, the number of degrees of freedom (DOF) increases substantially, and the modelling process becomes cumbersome from the user standpoint.

More recently, Sabatka et al. [14] have proposed a component-based finite element method to characterize the joints. This method takes into account all the real properties and dimensions of each part of the joint. The main difference with the method proposed in EC3 is that only bolts are modelled as translational springs, the other components, such as web panel, flanges and end-plate are modelled with shell finite elements. As a natural consequence, bending and shearing interaction in the panel is adequately addressed. However, this model has a considerable number of degrees of freedom and is mainly oriented to the analysis of individual joints and not to the global analysis of frames. For this purpose, it is necessary to condense and transform the complex model into a zero-length rotational spring, and as a consequence the transformation parameter β is needed again.

In order to avoid the use of the transformation parameter and to introduce joint dimensions, a 2D cruciform element with 4 nodes and 3 DOF per node was originally proposed by Bayo et al. [12] to model steel joints. The stiffness matrix of this element was generated from the stiffness defined in EC3 for each component. Additional cruciform elements have been developed such as: steel joints with beams of different depths [15], steel joints with trapezoidal panels [16, 17], composite joins [18], and a general cruciform element for joints with rectangular, trapezoidal and double rectangular panels [19]. All these elements adequately address the drawbacks mentioned before by considering the real dimensions of the joint, as well as the interaction between shear

and bending moments at the column panel, and therefore the β parameter is no longer necessary. Moreover, this 4-node cruciform element can be assembled with the rest of the elements (beams and columns) of the frame to perform a global analysis. However, the precision of this model is tied to the accuracy provided by the component method.

Joint modelling based on finite element models has proven to be very reliable and accurate [15, 16, 20, 21]. Analysis of local effects, corroboration of full-scale experiments and parametric studies are carried out straightforwardly and extensively using with FE packages. However, these analyses are expensive from a computational point of view and are not practical for day-to-day engineering work. In this context the use of surrogate modelling becomes an attractive possibility. Response surface methods (RSM), to construct surrogate models (metamodels), have been proposed as effective techniques to substitute expensive FE analyses. These studies address topics such as structural optimization [22], modelling of large scale structures [23], prediction of joint stiffness [24] and rotation capacity of wide flange beams [25]. Among all available RSM, the most frequently used are radial basis functions (RBF) [26], Kriging [27] and neural networks [28].

In this paper, the idea presented in [29] for welded connections has been extended and enhanced to develop a 4-node cruciform element for bolted extended end-plate connections. Due to the nonlinear phenomena arising from the contact between the end-plate and the column flange (not present in welded connections), the substructure process proposed in [29] is no longer feasible. Instead, the flexibility matrix of a 3-node cruciform element (see Fig. 1) is generated by applying unit forces and moments at the corresponding degrees of freedom. Then, and following standard procedures in matrix structural analysis [30], the flexibility matrix is transformed into the 12x12 complete stiffness matrix of a 4-node cruciform element (see Fig. 2). Next, singular values and eigenvectors (left and right), which constitute a reduced set of variables compared to the 144 variables of the full stiffness matrix, are calculated utilizing singular value

decomposition (SVD). Finally, the radial basis function (RBF) interpolation and Kriging's method are used to build a metamodel and predict the eigenvalues of the stiffness matrix.

The finite element modelling process that leads to the flexibility matrix, and some numerical examples that test the procedure are described in Section 2. Section 3 describes the parametric study and design of experiments (DOE), and how the surrogate model is built from SVD using RBF and Kriging methods. Then, numerical simulations that test and confirm the accuracy of the proposed method are presented in Section 4. Finally, Section 5 includes the concluding remarks.

2 FINITE ELEMENT MODEL AND 4-NODE CRUCIFORM ELEMENT

Simplified models of the joints can be obtained with mechanical models composed of zero-length springs. However, and as mentioned above, in this investigation Abaqus software was used to build a refined and accurate finite element of steel bolted extended end-plate connections. These models were used to characterize the flexibility matrix of the 3-node cruciform element shown in Fig. 1 in which the rotation and displacements (horizontal and vertical) at the base node are restrained. Then, following standard matrix structural procedures, the 3 DOF at the base were added to compute the complete stiffness matrix of the 4-node cruciform element depicted in Fig. 2.

2.1 Finite element model and flexibility matrix

The joint model consisted of two beams connected to a column through end-plates bolted to the column flanges and welded to the beam. End-plates were extended at the upper side of the column in order to provide the necessary resistance for hogging bending moments at both sides of the joint. Fig. 3 shows the geometry of the joint. The FE mesh was built using 8-node solid elements with reduced integration (to avoid shear locking) and hourglass control (C3D8R) (see Fig. 4). This way of modelling the joints with FE has been tested in previous investigations providing accurate results (see references [15–17]). Furthermore, five bolted steel connections

were simulated to compare the accuracy between the proposed FE modelling technique with previously performed experimental tests. The first connection is described in Faella et al. [11] as test "T101010". It is a single-sided extended end-plate connection with 6 bolts, IPE300 beam and HEB160 column. The next three are described in Augusto et al. [20] and referenced as tests "J-1.1", "J-3.1" and "J-4.1". They are double-sided extended end-plate connections with 8 bolts and the following combinations of beam and column profiles: IPE360-HEA320, IPE360-HEB320 and HEA280-HEA320, respectively. The last connection is a single-sided extended end-plate connection with 6 bolts, an IPE330 beam and a HEA300 column, which corresponds to the specimen A referred by Costa et al. [21]. The stiffness comparison is summarized in Table 1, where the results obtained using the component method of EC3 (reported in references [11,20,21]) are also included. It can be seen in Table 1 that there is a very good agreement between the results obtained with the FE models and the experimental results. In contrast, the results obtained with the component method are not as good.

The interactions between the different subassemblies of the FE model were solved using different types of constraints: the butt welds, between the beams and end-plates, were modelled using a tie kinematic constraint, the beam sections were defined as the slave surfaces while the end-plates were introduced as the master surface. This modelling technique was used with accuracy in previous researches as reported in [31, 32]. The interaction between the end-plate, the inner side of the column flange and the bolts were established with a “hard contact” constraint. In this model, both the normal and tangential forces were considered. The value adopted for the friction coefficient was $\mu = 0.3$. Finally, bolt preloading has been included by increasing the bolt elastic modulus according to procedure described in Jaspart et al. [33].

As shown in Fig. 4, for an IPE 450 beam and HEB 280 column, the steel sections were extended. This extension is necessary to take into account local phenomena and stress concentrations that occur near the joint. Nine configurations of beams and columns were tested

to identify the length of this zone. Each configuration was simulated with finite elements following the procedure mentioned above and extending the beams and column by 1 m. At the end of each beam, concentrated moments were applied to induce a hogging bending moment at the joint. As expected, the normal stress distribution was nonlinear near the joint in all the models. Using the normal stress plots, the zone where the Euler-Bernoulli stress distribution is not fulfilled was identified, and its length was defined as the value necessary for the extension. Fig. 5 shows the stress concentrations for the case 2 (see Annex A) with an IPE 300 beam and a HEB 220 combination. Table 2 shows the necessary length, and beam depth to length ratio for the models tested. It was observed from the stress distributions that an extension of $h/4$ (where h is the depth of the beam) for the lower part of the end-plate was enough to include the stress concentrations produced in the column web as well as the beam web and flange at the locations of the beam flanges. However, the *h/4* extension was too large for the upper part of the column and it was found that an extension of *h/8* was satisfactory for that part (the *h/8* extension was always measured from the upper edge of the end-plate).

As we were mainly concerned with the initial flexibility of the joint, steel was modelled as a linear elastic material. For the elastic modulus a value of 210 GPa was adopted, while for the Poisson ratio a value of 0.3 was applied. The complete finite element model depicted in Fig. 4 included 1,123,386 DOF.

In a previous study [29], the reduced stiffness matrix (12x12) of the model was computed with a linear perturbation step analysis of type “substructure”. However, due to the contact phenomena, this procedure is no longer possible. A flexibility procedure was then adopted to obtain the stiffness matrix of the cruciform element. First, four reference points (A, B, C and D) were defined, each one at the centre of gravity of each end section (see Fig. 4). Then, a rigid body kinematic constraint was introduced between each reference point and the section (surface) to which it belonged. Next, the degrees of freedom were restrained at the base reference point

(point A in Fig. 4) to define a fixed support. Finally, unit positive point loads and moments (following the numbering order shown in Fig. 1) were applied sequentially at each reference point. The displacements were measured at the DOFs for each unit load to form the columns of the flexibility matrix.

Due to the asymmetric configuration of the joint and contacts between parts, the actual joint behaviour and flexibility matrix depend upon the real distribution of forces and moments transmitted from each element to the joint. We need to know a priori the sign of the forces and moments so that, the corresponding flexibility columns can be properly selected. Therefore, with two possible directions at each degree of freedom (DOF), we would in principle need 9 x 2 flexibility columns. As a consequence, and to fully characterize the flexibility matrix, additional unit negative loads and moments were applied. Due to the symmetric behaviour of the loads applied at B and vertical loads applied at C and D, only 13 flexibility columns were needed for the simulations: the first 9 columns correspond to the positive values depicted in Fig.1, and the last four columns correspond to negative horizontal loads at nodes C (the axial tension) and D (the axial compression) and negative moments at nodes C (sagging moment) and D (hogging moment).

Finally, following standard matrix structural analysis procedures [30], the complete stiffness matrix of the 4-node cruciform element (Fig. 2) was calculated. As the flexibility matrix was of size 9 x 13, it had to be reduced to size 9 x 9. In this research, the joints tested in Section 2.2 were subjected to hogging bending moments, and therefore the 9 x 9 flexibility matrix was built using the first eight and last columns of the 9 x 13 matrix. The signs of the elements of this last column, obtained applying a negative moment at node D, were changed to be coherent with the global coordinate system used in the frame analysis.

2.2 Numerical examples

Two different frames (named Frame 1 and Frame 2) and three different loading conditions (named LC1, LC2 and LC3) for each frame were tested to check the precision of the method proposed above. The comparison was established by first analysing the frames using a detailed finite element model with Abaqus, and then by using a reduced structural model that included the 4-node cruciform element proposed above within Matlab. The frames were composed of two beams attached to columns (see Fig. 6). The length of the beams was 4.5 m, and the height of the columns was 3.5 m. The configuration for each structure, in terms of sections and dimensions of the joints, is summarized in Table 3. Three different loading conditions were considered for each of the frames, and the corresponding load values are shown in Table 4 for Frame 1, and Table 5 for Frame 2. The notation used for the loads is also illustrated in Fig. 6. Looking further into the three loading conditions, all of them included gravitational loads, and in loading condition 1 (LC1) there were no lateral loads. Loading condition 2 (LC2) included lateral loads but the gravitational load were dominant. In loading condition 3 (LC3) the lateral loads were the prevalent ones.

As already mentioned, each frame was initially solved by means of a complete finite element model using Abaqus. Fig. 7 shows the FE model, which contained 2,229,486 DOF. The modelling process, presented in Section 2.1, was again followed to construct the FE models. In this case, the kinematic surface constraints were imposed at the end of each element to enforce the following boundary conditions (see Fig. 6): fixed support at the bottom of the frame, double roller support with a rotation constraint at the top support, and a roller support at the end of each beam (left and right frame supports).

Then, following the procedure mentioned above, the stiffness matrix of the 4-node cruciform element (12x12 matrix) was computed and imported within Matlab. Afterwards, 2D beam and column structural elements (including axial, shear, and bending deformations) were assembled along with the cruciform element, using functions developed within Matlab, to form a

reduced structural model composed of 18 DOF (see Fig. 8). Finally, these frame models were subjected to the same loads as the FE model and solved using Matlab.

The comparison between the results obtained with Abaqus and Matlab was made with two different output data sets: reactions and displacements. The measured reactions are shown in Fig. 9. Table 6 shows that the maximum relative error (MRE) for the reactions is 1.4%. This value corresponds to the reaction R1 for loading condition LC3 and Frame 2. The accuracy provided by the Matlab models was also computed by means of the coefficient of determination R^2. This coefficient is defined as:

$$R^2 = 1 - \frac{\sum_{i=1}^{mv}(y_i - \hat{y}_i)^2}{\sum_{i=1}^{mv}(y_i - \bar{y}_i)^2} \quad (1)$$

where, y_i correspond to the Abaqus values with $\bar{y}_i$ being the mean value, $\hat{y}_i$ are the estimated values computed with Matlab, and mv is the number of data points. The closer R^2 is to the unit value the better the accuracy is. The results depicted in Table 6 indicate that the agreement between both models is excellent.

The second dataset composed of displacements also confirmed the good results obtained with the reactions. The displacements were measured at the nodes indicated in Fig. 10. As shown in Table 7, the MRE for the nodal displacements of Frame 1 was 0.8% for LC1, and 1.3% for Frame 2 with loading condition LC3. Also, the average relative error at these nodes is 0.6%. The minimum value of the R^2 parameter was 0.981 and the maximum 1. From these results, it is clear that both deflection shapes practically coincide with each other. Both datasets confirm that the 18 DOF reduced model that includes the proposed joint model provides results as accurate as those obtained with a complete FE model with 2.2 million DOFs.

3 METAMODEL

As mentioned above the finite element method is widely considered as a well-established technique capable of modelling the structural behaviour of steel joints and steel structures with accuracy and reliability. FE analyses can capture the global and local behaviour of joints. However, they are quite expensive from a computational point of view. For this reason, structural engineers prefer simpler models for their day-to-day frame analyses. Consequently, the aim is to provide a simplified model with the same level of precision as the complete finite element model. For this purpose, metamodeling techniques will be applied.

Our metamodel target is not the FE model, but the 4-node cruciform element proposed above. As demonstrated in the previous section, this 12 DOF element provides accuracy similar to that of the full FE models. However, it is necessary to address several issues to obtain an accurate metamodel of the stiffness matrix. These issues include: the sampling space and sampling strategy, the metamodeling process along with the response surface modelling technique, and the validation procedure.

3.1 Sampling space

For the correct definition of the surrogate model, it is customary to define a proper sampling space. This space is composed of two datasets of sample points: the training set and the validation set. Within the subject of Design of Experiments (DOE), there are numerous techniques for the choice of sampling spaces. The most used are the simple Rectangular Grid [27] and the Latin Hypercube [34]. The former one was used in this research due to its simplicity and adequate precision.

The sampling joint space was defined so as to cover 45 different combinations of IPE beam profiles and HEB columns. *Fig. 11* shows the subset used for the data experiment. For each of these combinations, three different configurations of bolt diameter (d_b) and end-plate thickness (t_p) were considered (see Annex A). The remaining parameters, corresponding to the

geometric disposition of the bolts, were estimated according to EC3, and the good steel construction practices indicated in steel joint design guides [35]. In total, 135 simulations were performed. 80% of these simulations are marked with empty circles in *Fig. 11* (which correspond to cases 1 and 3 of Annex A) and were used to build the training set that obtained the weights of the metamodel. The remaining 20% that are shown with filled circles in Fig. 10 (case 2 of Annex A) correspond to the validation set.

Following the procedure described in Section 2, the stiffness matrix (12x12) corresponding to the cruciform element was obtained for each of the data points. Subsequently, these matrices were factorized using singular value decomposition (SVD) to reduce the amount of data necessary for the surrogate model.

3.2 Singular value decomposition and the metamodel

The stiffness matrix of the bolted steel joint corresponds to a cruciform element of 4 nodes and 3 DOF per node. This renders a total of 144 elements for each matrix. Loureiro et al. [36] proposed to metamodel each matrix element as part of the surrogate model. However, this method demands a huge amount of data and computational resources. It has been shown in [29], that a modal approach based on eigenvalue decomposition considerably reduces the amount of data and therefore the size of the surrogate model.

Given the fact that the stiffness matrix is not symmetric we chose in this research, to use the singular value decomposition (SVD, which provides a very reliable and robust way of obtaining the deformation modes. The 12x12 stiffness matrix was decomposed using the "linalg.svd" function from Python Scipy package [37]. SVD decomposes the stiffness matrix into two orthonormal matrices: the left $\boldsymbol{U}$ and right $\boldsymbol{V}$ singular vectors, and a vector of singular values $\boldsymbol{\Sigma}$. Both, the $\boldsymbol{U}$ and $\boldsymbol{V}$ singular vectors can be interpreted as deformation modes. After analysing the singular vectors for several cases, the left vectors were identified as playing the same role as the eigenvectors in [29]. The first three modes represent the rigid-body motions, and

the other 9 were associated with the elastic deformation modes. The singular values characterize the stiffness of the corresponding vectors.

The singular value spectral decomposition satisfies the following relationship:

$$\boldsymbol{K} = \boldsymbol{U}\boldsymbol{\Sigma}\boldsymbol{V}^T \tag{2}$$

Therefore, a $\boldsymbol{K}$ matrix can be easily re-constructed from a given set of surrogate singular vectors, $\boldsymbol{U_s}$ and $\boldsymbol{V_s}$, and singular values $\boldsymbol{\Sigma_s}$ (the subscripts *s* stand for surrogate).

To understand the behaviour and classify the values ($\boldsymbol{\Sigma_s}$) and corresponding deformation modes ($\boldsymbol{U}$), a parametric study was carried out for the cases indicated in Fig. 11. As a result, 135 stiffness matrices were decomposed into singular values and singular vectors. To analyse the variation of each mode, the left singular vectors were previously clustered because singular values ordered from highest to lowest do not always correspond to the same modes. A K-means algorithm [38], developed in Python, was used for clustering each of the mode shapes.

The K-mean algorithm was fed with initial values for the centres of each cluster. These initial values are shown in Fig. 12. Each subplot corresponds to a deformation mode. The caption is an alias that indicates the predominant type of deformation caused by each mode. There are two shear modes: "ShearExt" and "ShearInt"; two bending modes: "BendBeam" and "BendCol"; two axial modes in the x direction: "AxialX" and "Axial2X"; two axial modes in the y direction: "AxialY" and "Axial2Y"; and finally an internal torsional mode "TorInt". Each bar corresponds to one component of the mode ($\boldsymbol{U}$ left singular vector). The component of each vector was normalized between 1 and -1. The bar labels correspond to the numbering of degrees of freedom shown in Fig. 1.

It was observed that the most relevant modes were "ShearExt", "BendBeam" and "BendCol". The amplified deformation produced by each of these modes is shown in Fig. 13. The singular values associated with these modes are the lowest ones. *Fig. 14* shows the singular values for the first three modes corresponding to the IPE 330 and a set of increasing HEB

column sizes (case 2 of Annex A). The remaining 6 modes have much higher singular values, quite far from those of the first 3 modes, as can be seen in Fig. 15. This implies that the participation of these last six modes in the overall behaviour of the joint is less significant than that of the first three modes.

After classifying each mode of the 135 connections, a statistical analysis was performed to evaluate the variation among modes for different connections. Fig. 16 shows a violin plot of the "ShearExt", "BendBeam" and "BendCol" modes. The modal components are all close to 0, except for the significant DOFs that are equal to 1 or - 1. However, the singular vectors of the remaining 6 modes are not as uniform as the first three, and have higher variability (see Fig. 17). However, if we study the variation within a cluster of connections, such as those indicated with dotted circles in Fig. 11 for the connection of Frame 1 and 2, the differences between the components are much smaller and the pattern becomes much more uniform.

Fig. 18 and 19 show the values of the "ShearInt" and "TorInt" modes for the groups of joints surrounding the joint of Frame 1 (HEB180-IPE330) and Frame 2 (HEB280-IPE450), respectively. It can be seen that the differences between the modal components are small. If we add to this the fact that these are very stiff modes and are not usually excited, it leads us to conclude that the modes ($\boldsymbol{U}$ left singular vector) do not need to be metamodelled since the approximation obtained using the closest modes is more than adequate. This hypothesis will be corroborated in Section 4 when performing the implementations and testing of two surrogate models. Therefore, the problem of metamodeling all the values of the 12x12 stiffness matrix can be reduced to that of metamodeling 9 singular values (only non-zero values) and storing the singular vectors, left $\boldsymbol{U}$ and right $\boldsymbol{V}$, of the training cases.

3.3 Surrogate modelling (RBF and Kriging)

Currently, there are numerous techniques to generate metamodels [27]: Kriging, neural networks, polynomial regression and radial basis functions (RBF), among others. In this study, the two methods RBF and Kriging were used.

The Kriging method predicts the value of the new sampled points as the sum of a random function, a stochastic process with zero average value, and a regression function [39]. The module *pyKriging* [40] was used in this research as the implementation of the Kriging method for Python. This module implements an algorithm to optimize the hyperparameters of the Kriging model: particle swarm (PS) and genetic algorithm (GA). For this research, the default option PS was used.

On the other hand, radial basis functions estimate the value of the new points from functions whose arguments are the distances of the new point to the sampling points of the data set [41]. Among all possible radial basis functions, the most standard are multiquadric, gaussian, inverse quadratic and inverse multiquadric. In this study, and after appropriate testing, multiquadric proved to be the best choice.

Initially, twelve features were chosen as parameters to build both metamodels: main dimensions of the column (depth, width and thickness of the web and flange), main dimensions of the beam (depth, width and thickness of the web and flange), the thickness of the plate, the bolt diameter, the vertical spacing between the bolts top rows p_{11} (see Fig. 3) and beam to column ratio. However, some of these parameters do not have the same influence on each eigenvalue. A GA was implemented in Python to identify the best features for each eigenvalue. To speed up this process, the RBF surrogate model was optimized with the GA. The parameters identified with GA were also used for the Kriging metamodel.

3.4 Validation of the surrogate model

The differences between the estimated and real values were quantified using three different values: the coefficient of determination R^2, the mean absolute percentage error (MAPE) and the root mean squared error (RMSE). These metrics provided enough information to assess the goodness of the model and the quality of the validation.

Table 8 shows the values of the R^2 coefficient, the MAPE and the RMSE applied to the validation set for the first three deformation modes and both metamodels, Kriging and RBF. Table 9 shows the same information for the last six modes. Concerning the values of R^2, it can be seen that almost all are equal to 1. The RMSE, with minimal values, show a good fit between the estimated and actual values. Finally, the MAPE values are also small with slightly higher values for the "ShearInt" and "Axil2X" modes. With these results, it is clear that both models, Kriging and RBF, are accurate enough and the model becomes well validated. As mentioned earlier, only the eigenvalues need to be metamodelled as the eigenvectors can be obtained from the surrounding cases.

4 TESTING OF THE SURROGATE MODEL

In Section 2.2, two frames were tested to validate the cruciform element using FE models. In this section, the same frames under the same loads were solved with Matlab. However, this time, the stiffness of the cruciform element was evaluated using the surrogate model. Comparison of both responses provided information about the fitness of the proposed method. The steel sections and loads were the same as before as shown in Tables 3-5 below.

The methods proposed in Section 3, RBF and Kriging, were used as surrogate modelling techniques. Using standard matrix structural analysis procedures, the metamodelled stiffness matrix was assembled into the stiffness matrix of the full frame. Then, the three loading conditions were applied. LC1 mostly excited the “BendBeam” mode of the joint stiffness; LC2 and LC3 predominantly excited both the “ShearExt” and “BendCol” modes.

Finally, as in Section 2.2, the displacements and reactions were analysed to identify the agreement between both models. The results for R^2 and MRE are summarised in Table 10 for the reactions, and in Table 11 for the displacements. The values of R^2 are close to 1 for all reactions and the maximum relative errors: 0.7% (RBF) and 0.8% (KRIG) occur in M4 for model 1 and load condition LC2. In the case of displacements, the R^2 values are again close to 1. The MRE for the Kriging surrogate is 0.4% for model 2 and load condition LC3. For the RBF surrogate model, the MRE is 0.5%. As shown for both datasets, the errors are very small, thus confirming the proposed method as sufficiently accurate and reliable.

5 CONCLUSIONS

The objective of this paper has been to develop a new cruciform element to model the stiffness of 2D steel bolted extended end-plate connections using surrogate models that are based on deformation modes. Standard structural analysis (Matlab) and FE simulations (Abaqus) were performed. From these analyses, the following conclusions are drawn:

1. The reduced 12x12 stiffness matrix of a 4-node cruciform element, corresponding to a steel bolted extended end-plate connection, can be accurately obtained using a flexibility substructuring process. The results of comparing the reactions and displacements of two subassemblies, modelled and solved with both the complete finite elements and the reduced stiffness, confirm the accuracy and suitability of the method.

2. The deformation modes of the 12x12 stiffness matrix differ very little for joints with similar dimensions. Accordingly, it is only necessary to metamodel the nine singular values, since the eigenvectors are recovered from those of the surrounding cases.

3. Factorization of the stiffness matrix through singular value decomposition considerably reduces the information to be metamodelled, without decreasing the accuracy provided by more complex FE models.

3. Both RBF and Kriging are excellent methods for metamodelling. However, Kriging is slightly more precise at the cost of a higher computational effort.

4. For the development of the sampling space, the uniform grid was chosen. 80% of the sample space was used for training the subrogate model, and the remaining 20% for validation.

5. The proposed methodology leads to a precise definition of the joint stiffness for frame analysis. This definition is valid for rigid as well as semi-rigid steel beam-to-column bolted extended end-plate connections. Furthermore, the proposed technique is easy to implement in structural analysis programs.

ACKNOWLEDGEMENTS

The financial support provided by the Spanish Ministerio de Economía, Industria y Competitividad-Agencia Estatal de Investigación y Fondo Europeo de Desarrollo Regional under contract BIA2016-80358-C2-1-P MINECO/FEDER UE and by the University of Oviedo under contract 2020/00024/024 are gratefully acknowledged.

ANNEX A

HEB	IPE	Case 1		Case 2		Case 3	
		t_p	d_b	t_p	d_b	t_p	d_b
160	140	9	M12	11	M12	14	M12
	180	10	M12	13	M12	16	M16
	220	11	M12	14	M16	17	M16
	270	12	M16	15	M16	19	M20
	330	14	M16	17	M20	21	M20
180	160	10	M12	12	M12	15	M12
	200	11	M12	14	M12	17	M16
	240	12	M16	15	M16	18	M16
	300	13	M16	17	M20	20	M20
	360	15	M20	19	M20	23	M22
200	180	11	M12	13	M16	16	M16
	220	12	M12	15	M16	18	M16
	270	13	M16	16	M20	20	M20
	330	15	M16	18	M20	22	M20
	400	16	M20	20	M20	24	M22
220	200	12	M12	15	M16	18	M16
	240	13	M16	16	M16	19	M16
	300	14	M16	18	M20	21	M20
	360	16	M20	20	M20	24	M22
	450	17	M20	20	M20	24	M22
240	220	13	M16	16	M16	19	M16
	270	14	M16	17	M20	21	M20
	330	15	M20	19	M20	23	M20
	400	16	M20	20	M22	25	M24
	500	17	M22	21	M22	26	M24
260	240	14	M16	17	M16	20	M16
	300	15	M16	19	M20	21	M20
	360	17	M20	21	M20	24	M24
	450	18	M20	20	M22	22	M24
	550	18	M22	23	M24	28	M27
280	270	15	M16	18	M20	22	M20
	330	16	M20	20	M20	24	M22
	400	17	M20	21	M22	26	M24
	500	18	M22	22	M22	27	M24
	600	18	M22	22	M24	28	M27
300	300	16	M20	20	M20	22	M20
	360	18	M20	22	M20	25	M24
	450	19	M20	20	M22	24	M24
	550	20	M20	24	M24	27	M27
	750x137	21	M22	25	M24	28	M27
320	330	17	M20	21	M20	25	M22
	400	18	M20	22	M22	27	M24
	500	19	M22	23	M24	26	M24
	600	20	M22	24	M24	28	M27
	750x137	21	M22	25	M24	29	M27

REFERENCES

[1] CEN, Eurocode 3: Design of steel structures. Part 1.1: General Rules and Rules for Building, 2005.

[2] CEN, Eurocode 3: Design of Steel Structures. Part 1.8: Design of Joints, 2005.

[3] AISC, Steel Construction Manual, 14th ed., American Institute of Steel Construction, 2011.

[4] W.F. Chen, N. Kishi, K. Matsuoka, S. Nomachi, Moment–rotation relation of single double web angle connections. Connections in steel structures: behaviour, strength and design, in: Proc. State Art Work. Connect. Behav. Strength Des. Steel Struct., Elsevier, London, 1988: pp. 135–149.

[5] M.J. Frye, G.A. Morris, Analysis of Flexibly Connected Steel Frames, Can. J. Civ. Eng. 2 (1975) 280–291. https://doi.org/10.1139/l75-026.

[6] H. Krawinkler, Shear in beam-column joints in seismic design of steel frames, Eng. J. 15 (1978) 82–91.

[7] M. Ivanyi, C.C. Baniotopoulos, Semi-Rigid Joints in Structural Steelwork, in: M. Ivanyi, C.C. Baniotopoulos (Eds.), Semi-Rigid Joints Struct. Steelwork, Springer Vienna, Vienna, 2000: pp. 1–101. https://doi.org/10.1007/978-3-7091-2478-9.

[8] W.F. Chen, Practical Analysis for Semi-Rigid Frame Design, World Scientific Publishing Company, 2000. https://doi.org/10.1142/4277.

[9] J.M. Castro, A.Y. Elghazouli, B.A. Izzuddin, Modelling of the panel zone in steel and composite moment frames, Eng. Struct. 27 (2005) 129–144. https://doi.org/10.1016/j.engstruct.2004.09.008.

[10] A. Daniunas, K. Urbonas, Analysis of the steel frames with the semi-rigid beam-to-beam and beam-to-column knee joints under bending and axial forces, Eng. Struct. 30 (2008) 3114–3118. https://doi.org/10.1016/j.engstruct.2008.04.027.

[11] C. Faella, V. Piluso, G. Rizzano, Structural steel semirigid connections : theory, design, and software, CRC Press, 2000.

[12] E. Bayo, J.M. Cabrero, B. Gil, An effective component-based method to model semi-rigid connections for the global analysis of steel and composite structures, Eng. Struct. 28 (2006) 97–108. https://doi.org/10.1016/j.engstruct.2005.08.001.

[13] SSEDTA, Eurocodes for Composite Structures. Structural Steelwork Eurocodes Development of a transnational approach. Module 4: Joints, 2001.

[14] L. Sabatka, F. Wald, J. Kabeláč, L. Gödrich, J. Navrátil, Component based finite element model of structural connections, in: Proc. 12th Int. Conf. Steel, Sp. Compos. Struct., Prague, 2014: pp. 337–344.

[15] A. Loureiro, M. Lopez, E. Bayo, Shear behaviour of stiffened double rectangular column panels: Characterization and cruciform element, J. Constr. Steel Res. 117 (2016) 126–138. https://doi.org/10.1016/j.jcsr.2015.10.012.

[16] E. Bayo, A. Loureiro, M. Lopez, Shear behaviour of trapezoidal column panels. I: Experiments and finite element modelling, J. Constr. Steel Res. 108 (2015) 60–69. https://doi.org/10.1016/j.jcsr.2014.10.026.

[17] M. Lopez, A. Loureiro, E. Bayo, Shear behaviour of trapezoidal column panels. II: Parametric study and cruciform element, J. Constr. Steel Res. 108 (2015) 70–81. https://doi.org/10.1016/j.jcsr.2014.10.029.

[18] E. Bayo, J. Gracia, B. Gil, R. Goñi, An efficient cruciform element to model semirigid composite connections for frame analysis, J. Constr. Steel Res. 72 (2012) 97–104. https://doi.org/10.1016/j.jcsr.2011.11.006.

[19] E. Bayo, A. Loureiro, M. Lopez, L. Simões da Silva, General component based cruciform finite elements to model 2D steel joints with beams of equal and different depths, Eng. Struct. 152 (2017) 698–708. https://doi.org/10.1016/j.engstruct.2017.09.042.

[20] H. Augusto, L. Simões da Silva, C. Rebelo, J.M. Castro, Characterization of web panel components in double-extended bolted end-plate steel joints, J. Constr. Steel Res. 116 (2016) 271–293. https://doi.org/10.1016/j.jcsr.2015.08.022.

[21] R. Costa, J. Valdez, S. Oliveira, L. Simões da Silva, E. Bayo, Experimental behaviour of 3D end-plate beam-to-column bolted steel joints, Eng. Struct. 188 (2019) 277–289. https://doi.org/10.1016/j.engstruct.2019.03.017.

[22] S. Sakata, F. Ashida, M. Zako, Structural optimizatiion using Kriging approximation, Comput. Methods Appl. Mech. Eng. (2003). https://doi.org/10.1016/S0045-7825(02)00617-5.

[23] L. Zhou, G. Yan, J. Ou, Response Surface Method Based on Radial Basis Functions for Modeling Large-Scale Structures in Model Updating, Comput. Civ. Infrastruct. Eng. 28 (2013) 210–226. https://doi.org/10.1111/j.1467-8667.2012.00803.x.

[24] L.R.O. de Lima, P.C.G. da S. Vellasco, S.A.L. de Andrade, J.G.S. da Silva, M.M.B.R. Vellasco, Neural networks assessment of beam-to-column joints, J. Brazilian Soc. Mech. Sci. Eng. 27 (2005) 314–324. https://doi.org/10.1590/S1678-58782005000300015.

[25] I.H. Guzelbey, A. Cevik, M.T. Gögüş, Prediction of rotation capacity of wide flange beams using neural networks, J. Constr. Steel Res. 62 (2006) 950–961. https://doi.org/10.1016/j.jcsr.2006.01.003.

[26] A.A. Mullur, A. Messac, Metamodeling using extended radial basis functions: A comparative approach, Eng. Comput. 21 (2006) 203–217. https://doi.org/10.1007/s00366-005-0005-7.

[27] A.I.J. Forrester, A. Sóbester, A.J. Keane, Engineering Design via Surrogate Modelling, Wiley, 2008. https://doi.org/10.1002/9780470770801.

[28] M.R. Sheidaii, R. Bahraminejad, Evaluation of compression member buckling and post-buckling behavior using artificial neural network, J. Constr. Steel Res. 70 (2012) 71–77. https://doi.org/10.1016/j.jcsr.2011.10.020.

[29] E. Bayo, J. Gracia, Stiffness modelling of 2D welded joints using metamodels based on mode shapes, J. Constr. Steel Res. 156 (2019) 242–251. https://doi.org/10.1016/j.jcsr.2019.02.017.

[30] W. McGuire, R.H. Gallagher, R.D. Ziemian, Matrix structural analysis, John Wiley, 2000.

[31] B. Gil, R. Goñi, T-stub behaviour under out-of-plane bending. I: Experimental research and finite element modelling, Eng. Struct. 98 (2015) 230–240. https://doi.org/10.1016/j.engstruct.2015.03.041.

[32] B. Gil, R. Goñi, E. Bayo, Initial stiffness and strength characterization of minor axis T-stub under out-of-plane bending, J. Constr. Steel Res. 140 (2018) 208–221. https://doi.org/10.1016/j.jcsr.2017.10.028.

[33] J.P. Jaspart, R. Maquoi, Effect of bolt preloading on joint behaviour, in: Proc. First Eur. Conf. Steel Struct., Athénes, 1995: pp. 219–226. http://hdl.handle.net/2268/30588.

[34] M.D. McKay, R.J. Beckman, W.J. Conover, A comparison of three methods for selecting values of input variables in the analysis of output from a computer code, Technometrics.

42 (2000) 55–61. https://doi.org/10.1080/00401706.2000.10485979.

[35] T. Murray, L. Shoemaker, Design Guide 16: Flush and Extended Multiple-Row Moment End-Plate Connections, American Institute of Steel Construction, 2002. https://www.aisc.org/Design-Guide-16-Flush-and-Extended-Multiple-Row-Moment-End-Plate-Connections.

[36] A. Loureiro, M. Lopez, J.M. Reinosa, R. Gutierrez, E. Bayo, Metamodelling of stiffness matrices for 2D welded asymmetric steel joints, J. Constr. Steel Res. (2019). https://doi.org/10.1016/j.jcsr.2019.105703.

[37] P. Virtanen, R. Gommers, T.E. Oliphant, M. Haberland, T. Reddy, D. Cournapeau, E. Burovski, P. Peterson, W. Weckesser, J. Bright, S.J. van der Walt, M. Brett, J. Wilson, K. Jarrod Millman, N. Mayorov, A.R.J. Nelson, E. Jones, R. Kern, E. Larson, C.J. Carey, I. Polat, Y. Feng, E.W. Moore, J. Vand erPlas, D. Laxalde, J. Perktold, R. Cimrman, I. Henriksen, E.A. Quintero, C.R. Harris, A.M. Archibald, A.H. Ribeiro, F. Pedregosa, P. van Mulbregt, SciPy 1.0: Fundamental Algorithms for Scientific Computing in Python, Nat. Methods. 17 (2020) 261–272. https://doi.org/https://doi.org/10.1038/s41592-019-0686-2.

[38] T. Kanungo, D.M. Mount, N.S. Netanyahu, C.D. Piatko, R. Silverman, A.Y. Wu, An efficient k-means clustering algorithms: Analysis and implementation, IEEE Trans. Pattern Anal. Mach. Intell. 24 (2002) 881–892. https://doi.org/10.1109/TPAMI.2002.1017616.

[39] S.N. Lophaven, J. Søndergaard, H.B. Nielsen, DACE - A Matlab Kriging Toolbox, (2002) 28. http://www2.imm.dtu.dk/pubdb/views/publication_details.php?id=1460.

[40] C. Paulson, G. Ragkousis, pyKriging: A Python Kriging Toolkit, (2015). https://doi.org/10.5281/zenodo.21389.

[41] R.L. Hardy, Multiquadric equations of topography and other irregular surfaces, J. Geophys. Res. 76 (1971) 1905–1915. https://doi.org/10.1029/JB076i008p01905.

TABLES

Table 1. Comparison between FE models and experimental tests

	Experimental stiffness (kN.m)	**FEM stiffness (kN.m)**	**Error (%)**	**EC3 stiffness (kN.m)**	**Error (%)**
Faella et al T101010	25.316	23.200	8.3%	20.856	17.6%
Augusto et al J1.1	71.340	66.880	6.3%	60.246	15.6%
Augusto et al J3.1	95.057	87.620	7.8%	72.950	23.3%
Augusto et al J4.1	38.495	36.480	5.3%	37.865	1.6%
Costa et al Spec. A	53.705	51.900	3.4%	37.380	30.4%

Table 2. Length of the region of stress concentrations and beam depth to length ratio (dimensions in mm)

	HEB 160 IPE 220	**HEB 180 IPE 240**	**HEB 200 IPE 270**	**HEB 220 IPE 300**	**HEB 240 IPE 330**	**HEB 260 IPE 360**	**HEB 280 IPE 400**	**HEB 300 IPE 450**	**HEB 320 IPE 500**
Length	55.0	60.0	70.0	74.0	87.2	91.0	99.4	115	128.8
Beam depth / length	4.0	4.0	3.85	4.05	3.78	3.95	4.02	3.91	3.88

Table 3. Frame configurations (dimensions in mm)

	Column	**Beam**	$\mathbf{d_0}$	$\mathbf{t_p}$	$\mathbf{e_{11}}$	$\mathbf{p_{11}}$	$\mathbf{p_{12}}$	$\mathbf{e_{12}}$	$\mathbf{e_2}$	$\mathbf{p_2}$
Frame 1	HEB 180	IPE 330	M20	16	38	88	231	70	38	86
Frame 2	HEB 280	IPE 450	M22	20	40	95	341	75	40	102

Table 4. Loading combinations for Frame 1

	$\mathbf{F_1}$ **(KN)**	$\mathbf{F_2}$ **(KN)**	$\mathbf{F_3}$ **(KN)**	$\mathbf{q_1}$ **(KN/m)**	$\mathbf{q_2}$ **(KN/m)**
LC1	0	0	-300	-75	-75
LC2	22	11	-300	-50	-50
LC3	30	15	-150	-25	-25

Table 5. Loading combinations for Frame 2

	$\mathbf{F_1}$ **(KN)**	$\mathbf{F_2}$ **(KN)**	$\mathbf{F_3}$ **(KN)**	$\mathbf{q_1}$ **(KN/m)**	$\mathbf{q_2}$ **(KN/m)**
LC1	0	0	-500	-150	-150
LC2	50	25	-500	-100	-100
LC3	80	40	-400	-50	-50

Table 6. Comparison of reactions between the Abaqus model and the reduced Matlab model

	Frame 1			**Frame 2**		
	LC1	**LC2**	**LC3**	**LC1**	**LC2**	**LC3**
R^2	1.000	1.000	1.000	1.000	1.000	1.000
MRE %	0.0	0.4	0.6	0.3	0.5	1.4

Table 7. Comparison of displacement between the Abaqus model and the reduced Matlab model

	Frame 1			**Frame 2**		
	LC1	**LC2**	**LC3**	**LC1**	**LC2**	**LC3**
R^2	0.981	0.998	1.000	1.000	1.000	0.999
MRE %	0.8	0.3	0.1	0.6	0.7	1.3

Table 8. RMSE, R2 and MAPE obtained with Kriging and RBF metamodels for the first three deformation modes

	ShearExt		**BendCol**		**BendBeam**	
Metamodel	KRIG.	RBF	KRIG.	RBF	KRIG.	RBF
RMSE	0.003	0.002	0.013	0.009	0.009	0.012
R^2	1.000	1.000	0.999	1.000	1.000	1.000
MAPE %	0.176	0.160	0.689	0.224	0.617	0.712

Table 9. RMSE, R2 and MAPE obtained with Kriging and RBF metamodels for the last six deformation modes

	TorInt		**ShearInt**		**AxilY**		**AxilX**		**Axil2Y**		**Axil2X**	
Metamodel	KRIG.	RBF	KRIG.	RBF	KRIG.	RBF	KRIG.	RBF	KRIG.	RBF	KRIG.	RBF
RMSE	0.014	0.012	0.046	0.030	0.003	0.004	0.003	0.002	0.004	0.005	0.039	0.015
R2	0.995	0.996	0.949	0.979	0.999	0.999	1.000	1.000	1.000	0.999	0.955	0.993
MAPE %	1.027	0.901	3.221	2.698	0.249	0.294	0.194	0.091	0.273	0.385	2.953	1.268

Table 10. Comparison of reactions between the complete and surrogate models

	Frame 1						**Frame 2**					
	LC1		**LC2**		**LC3**		**LC1**		**LC2**		**LC3**	
	KRIG.	RBF	KRIG.	RBF	KRIG.	RBF	KRIG.	RBF	KRIG.	RBF	KRIG.	RBF
R^2	1.000	1.000	1.000	1.000	1.000	1.000	1.000	1.000	1.000	1.000	1.000	1.000
MRE %	0.1	0.2	0.7	0.8	0.4	0.4	0.1	0.1	0.4	0.5	0.4	0.5

Table 11. Comparison of displacement between the complete and surrogate models

	Frame 1						**Frame 2**					
	LC1		**LC2**		**LC3**		**LC1**		**LC2**		**LC3**	
	KRIG.	RBF	KRIG.	RBF	KRIG.	RBF	KRIG.	RBF	KRIG.	RBF	KRIG.	RBF
R^2	1.000	1.000	1.000	1.000	1.000	1.000	1.000	1.000	0.999	0.999	1.000	1.000
MRE %	0.3	0.5	0.2	0.1	0.2	0.2	0.2	0.3	0.3	0.1	0.4	0.2

FIGURES

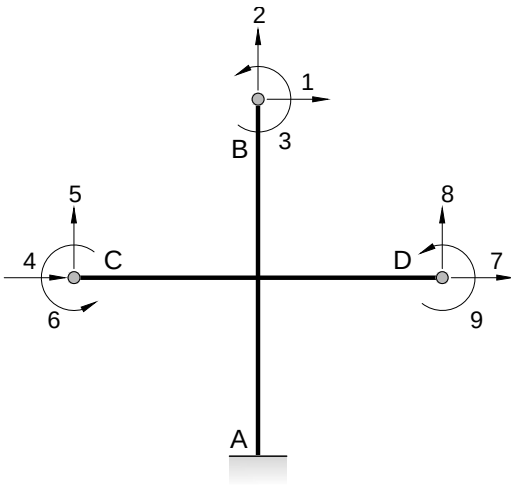

Fig. 1. 3-node, 9 DOF cruciform element

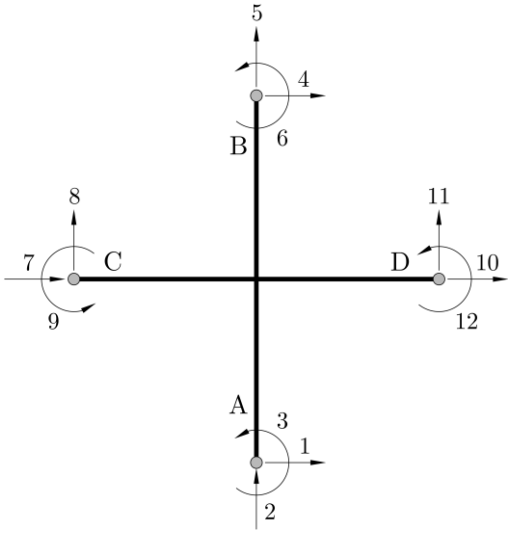

Fig. 2. 4-node, 12 DOF cruciform element

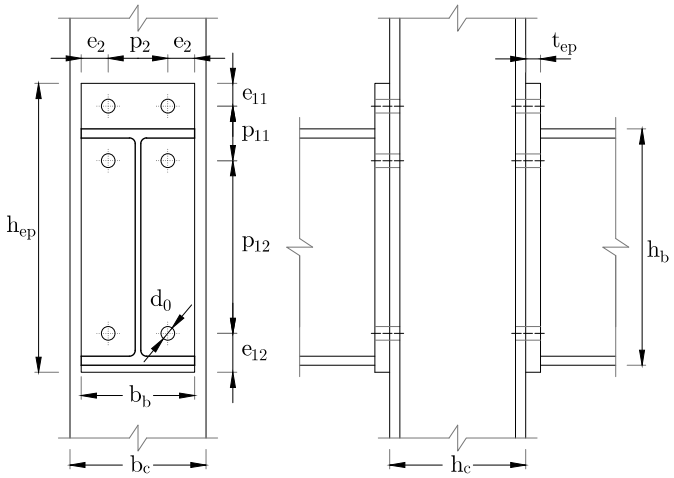

Fig. 3. Geometric parameters of the bolted extended end-plate connection

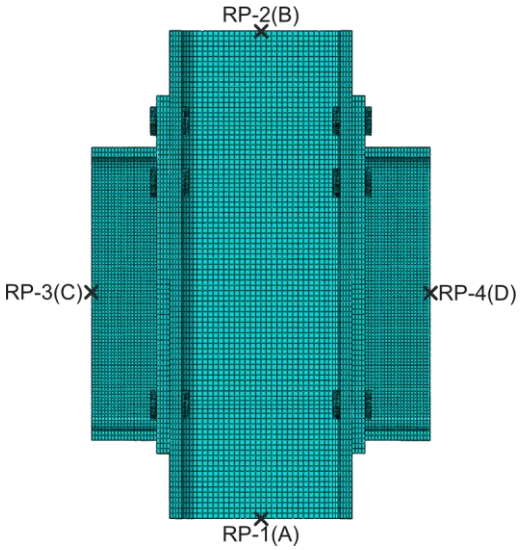

Fig. 4. Detail of the finite element model and location of the reference points

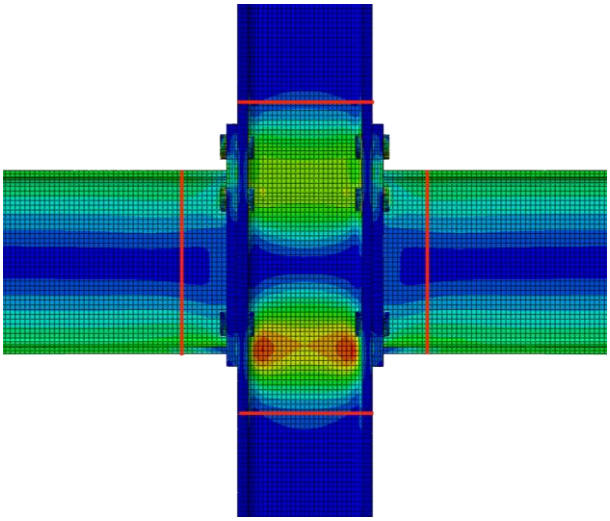

Fig. 5. Stress concentrations for Case 2 (see Annex A) with a HEB 220 and IPE 300 combination

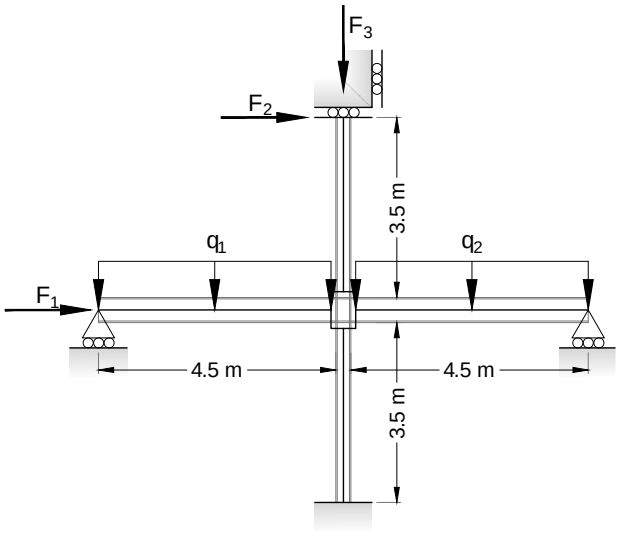

Fig. 6. Frame and loads considered in the simulations

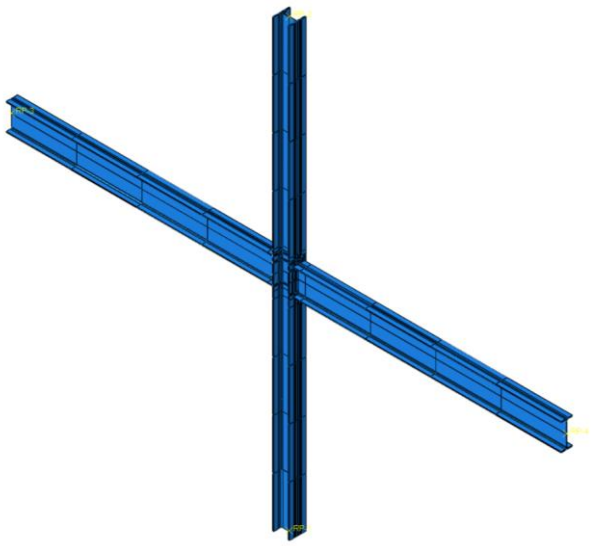

Fig. 7. Complete finite element model of Frame 1

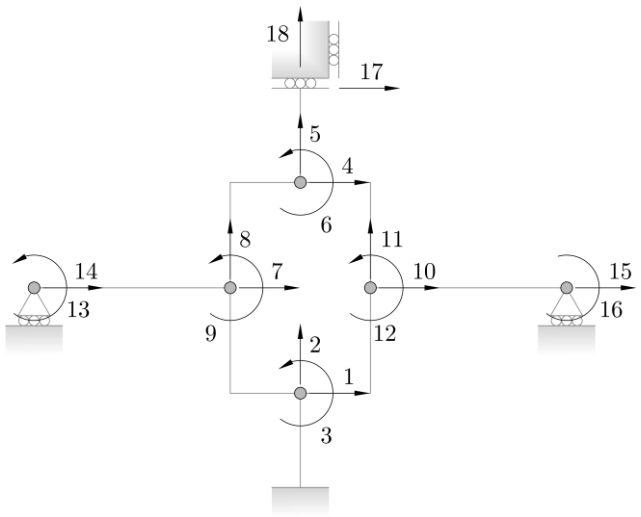

Fig. 8. Matlab structural model and DOF, including the cruciform element

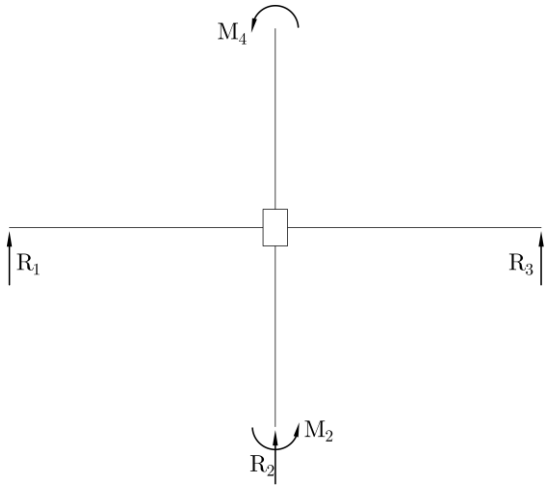

Fig. 9. Measured reactions

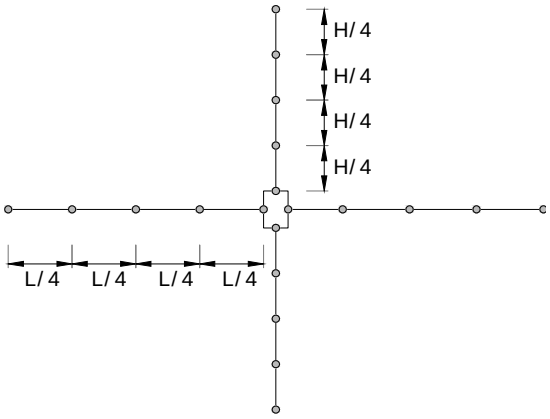

Fig. 10. Structural nodes where the total displacement were measured

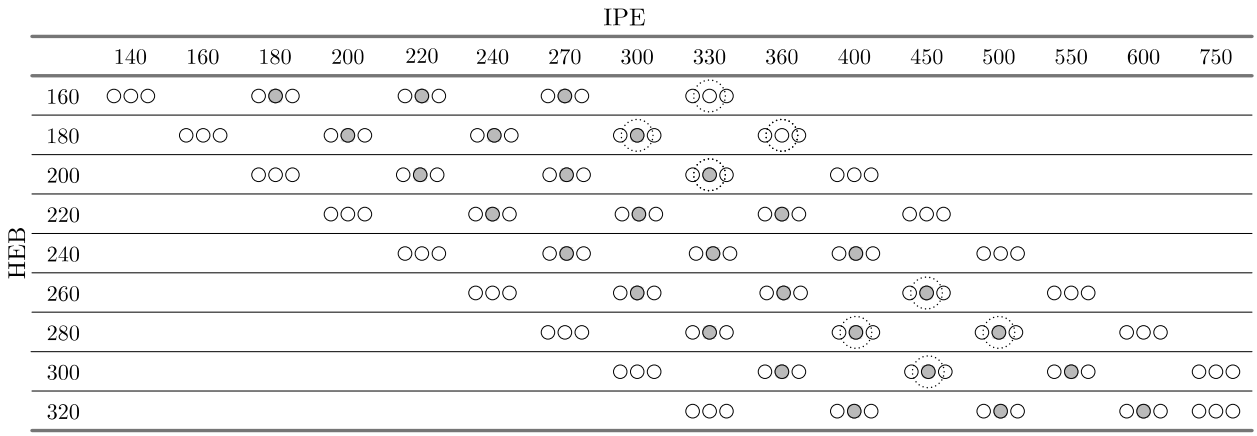

Fig. 11. Data set: Uniform Grid of columns (HEB) and beams (IPE)

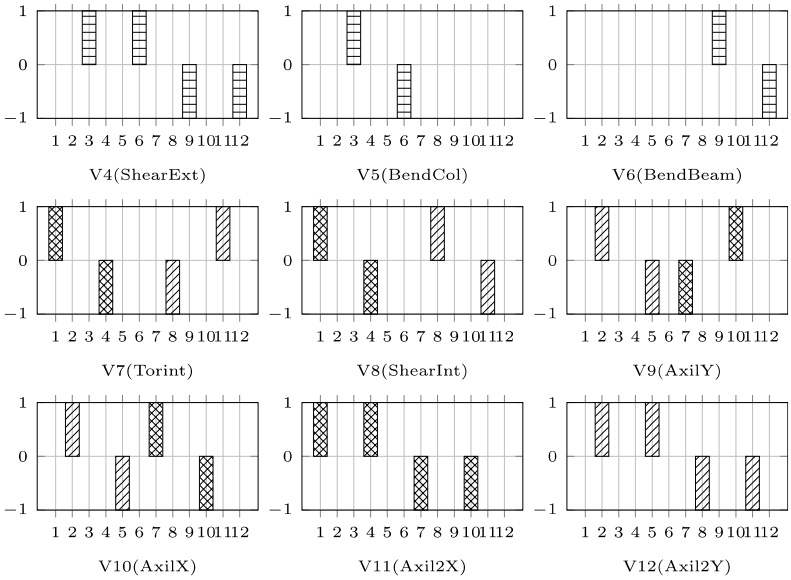

Fig. 12. Deformation modes

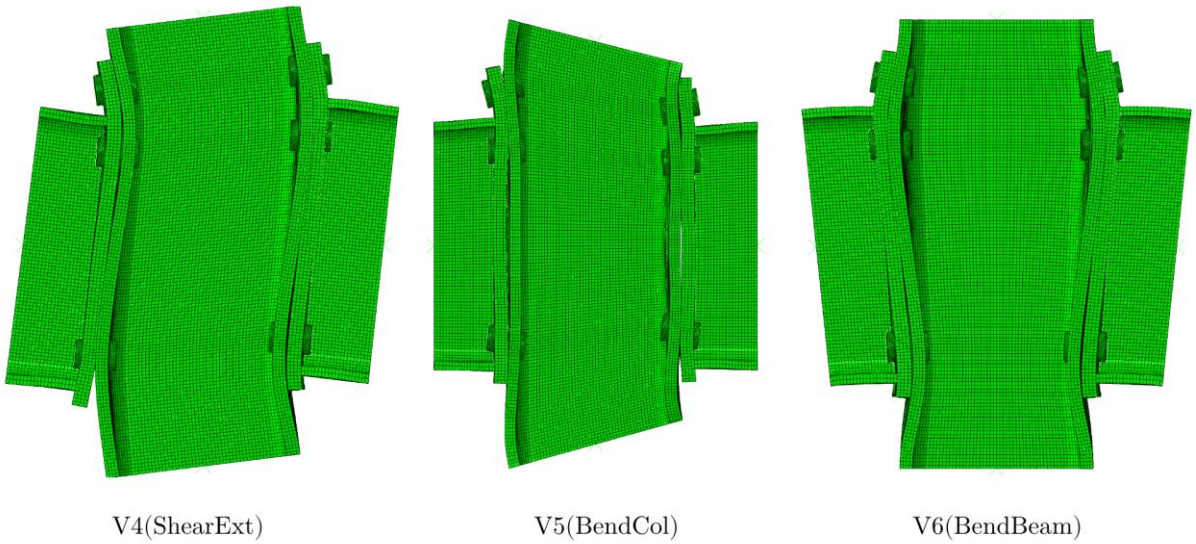

Fig. 13. Most significant mode shapes

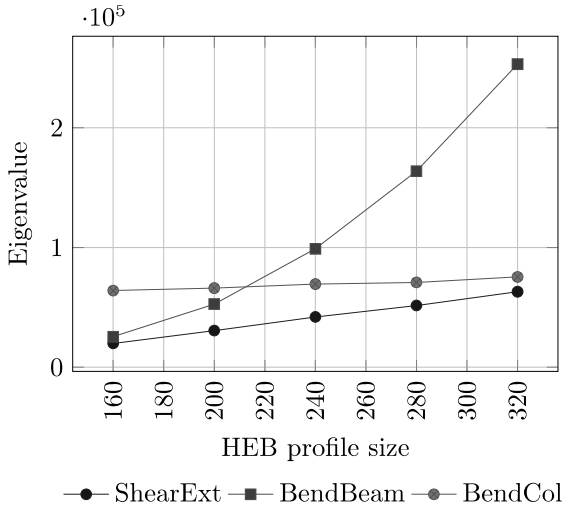

Fig. 14. Singular values of the first three modes for IPE330 and increasing HEB sizes

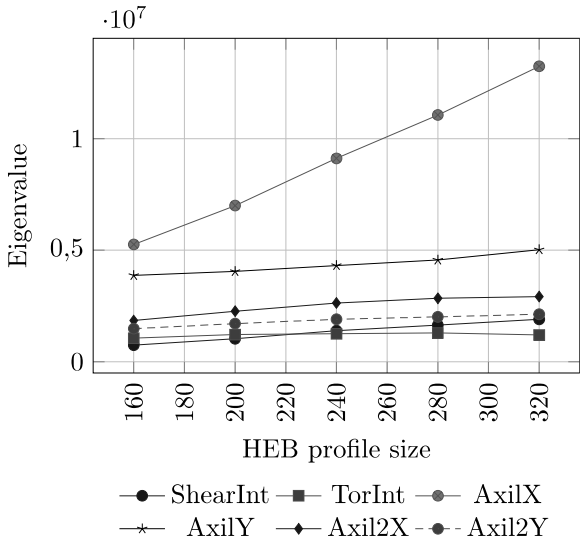

Fig. 15. Singular values of the stiffer modes for IPE330 and increasing HEB sizes

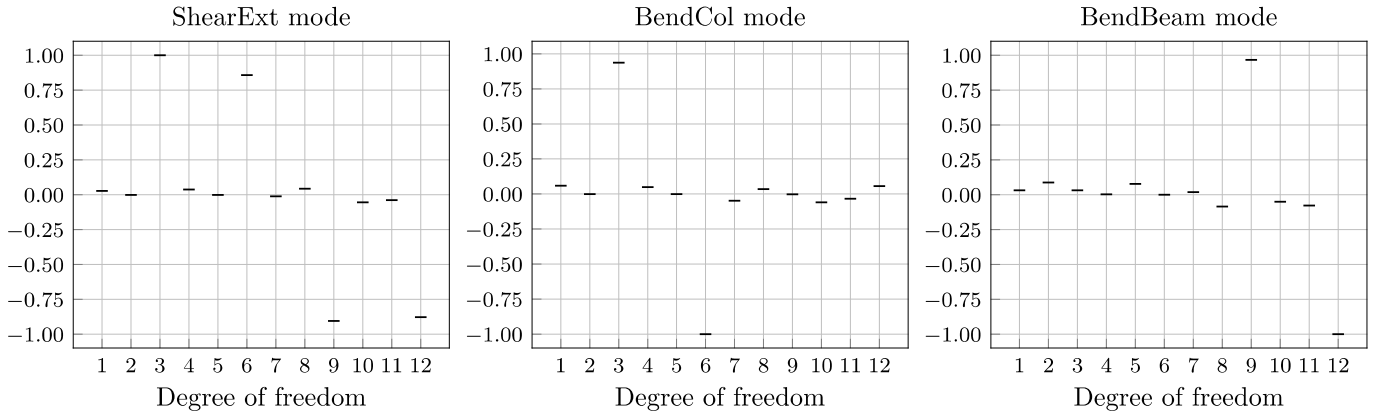

Fig. 16. Violin plots for the "ShearExt", "BendBeam" and "BendCol" modes

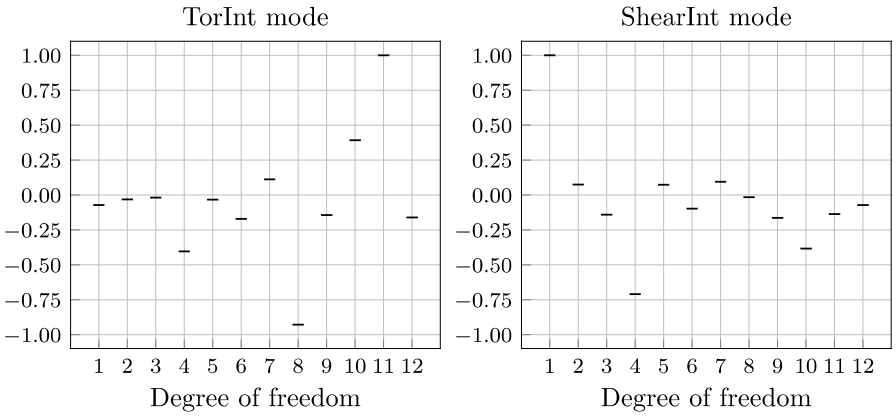

Fig. 17. Violin plots for the "ShearInt" and "TorInt" modes

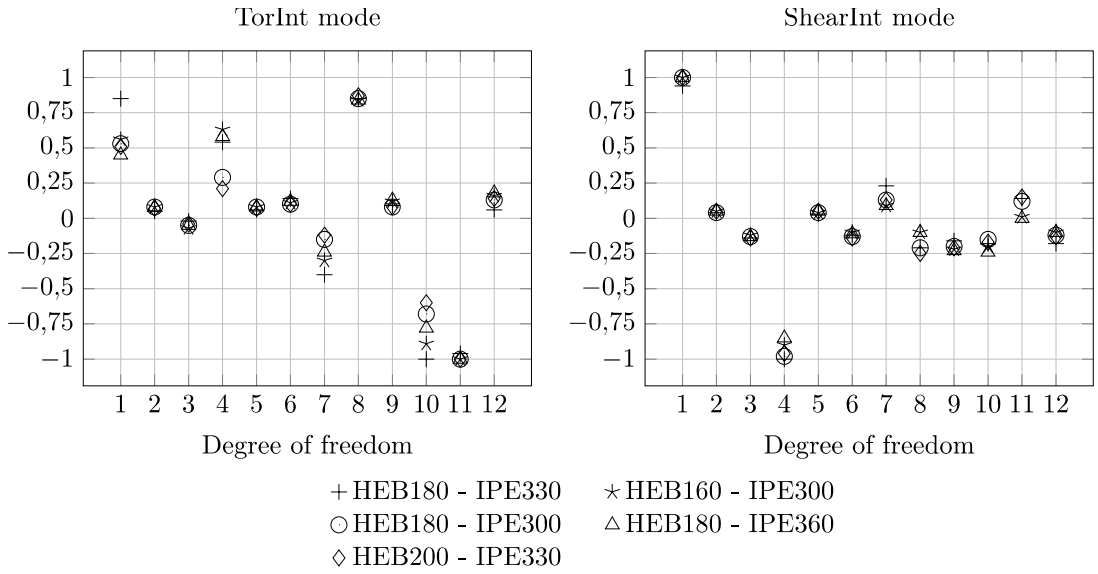

Fig. 18. Surrounding cases for "ShearInt" and "TorInt" modes in Frame 1

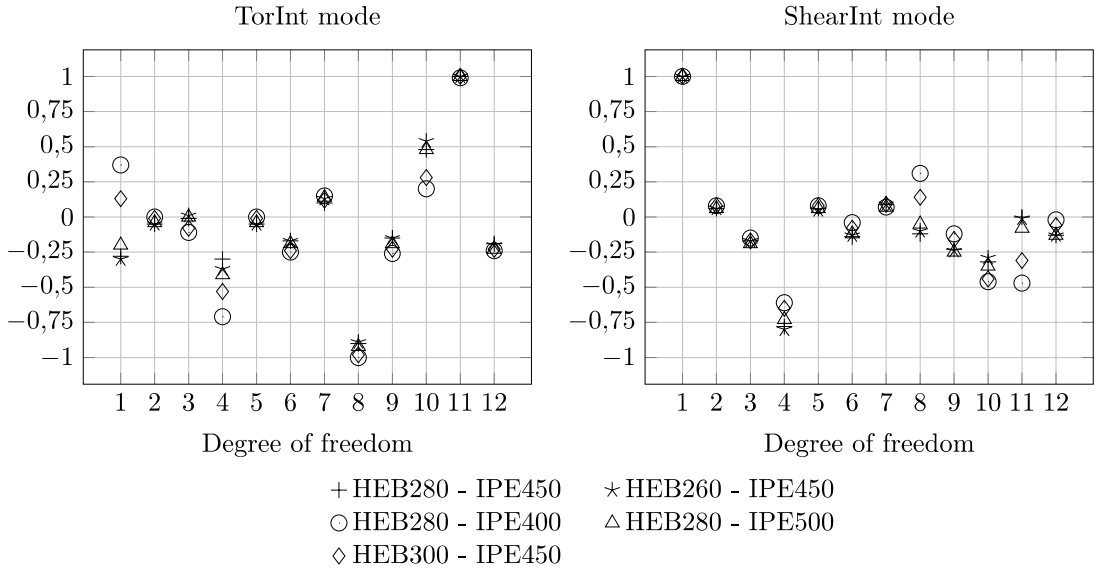

Fig. 19. Surrounding cases for "ShearInt" and "TorInt" modes in Frame 2